

TWENTY-FIFTH EUROPEAN ROTORCRAFT FORUM

Paper Number C7

**Large-Eddy Simulation of
Unsteady Rotor Aerodynamics and Acoustics Emission**

BY

C. Berbente, S. Mitran
Faculty of Aerospace Engineering
"politecnica" University Bucarest

SEPTEMBER 14-16, 1999
ROME
ITALY

Large-Eddy Simulation of Unsteady Rotor Aerodynamics and Acoustic Emissions

C. Berbente, S. Mitran
Faculty of Aerospace Engineering
“Politehnica” University Bucharest
Spl. Independentei 313, Sector 6
RO-77206, Bucharest, Romania

July 13, 1999

1 Introduction

In this paper we report on the development of a novel numerical procedure that has been applied to the study of unsteady rotor flow. The method uses an essentially multidimensional, residual distribution approach [3] on unstructured tetrahedral grids. An eigenmode analysis of the convective part of the flow equations furnishes a truly multidimensional procedure to split residuals on each cell so as to ensure upwinding. Turbulent effects are included by LES with an adaptation of Germano dynamic subgrid scale stress model. Multigrid acceleration, based upon a sequence of nested tetrahedral grids, is used to accelerate the computation. The adaptation of the Germano SGS model is applied at each multigrid level, thus acting as a physically based prolongation and restriction operator for the viscous part of the multigrid procedure. This adaptation together with the eigenmode based residual distribution procedure serve to ensure good acceleration properties from the multigrid procedure. The code implementing these concepts has been developed by the second author and is named OCTLES (<http://www.propulsion.pub.ro/OCTLES/index.html>). The code has been validated on a number of the LES test cases suggested in a recent AGARD report on this subject [2]. The test cases included flows with secondary effects such as rotation and curvature.

An application to the case of a twisted rotor blade is presented. The tip is in transonic flow and a portion of the inboard part of the blade has stalled flow. The capabilities of the code to simulate this complicated, three dimensional flow field are well demonstrated by this test case. After presentation of the three-dimensional flow a two-dimensional blade vortex interaction problem is studied with a view to establishing possible benefits of using porous airfoils. The Kirchhoff surface technique is used to compute the far field acoustic radiation. Computation of the Kirchhoff integrals is carried out by solving an equivalent initial value problem. This has

the advantage of allowing full space and time adaptivity and thus lowering computational costs. Typical acoustic signatures are presented. There appears to be a modest benefit to be gained by use of porous airfoils, with a reduction of 10-15% of peak acoustic pressure being observed in some cases. There is increased spectral content in the acoustic signature. This is thought to be associated modification of the shock structures on the porous airfoil.

2 Numerical procedures

2.1 Residual distribution schemes

Most of the numeric discretization procedures that are in wide-spread use today are extensions of schemes derived for the one-dimensional flow equations. These are then extended to multidimensional flow, typically by directional splitting. This introduces a numerical bias in the essentially three-dimensional flow physics. Recently, a number of investigations have addressed the problem of obtaining a true multidimensional description of flow phenomena. Current research activity at the Faculty of Aerospace Engineering, "Politehnica" University, Bucharest is focused on these types of schemes with encouraging initial results [6]. Since the important part of the flow equations for ensuring multidimensional discretization is the convection operator the theoretical development is carried out for the Euler equations.

$$q_t + f_x + g_y + h_z = 0, \quad q = [\rho \quad l \quad m \quad n \quad \varepsilon]^T \quad (1)$$

$$l = \rho u, \quad m = \rho v, \quad n = \rho w, \quad \varepsilon = \rho E = \rho e + \rho \frac{u^2 + v^2 + w^2}{2} \quad (2)$$

$$f = \begin{bmatrix} l \\ p + l^2/\rho \\ lm/\rho \\ ln/\rho \\ l(p + \varepsilon)/\rho \end{bmatrix}, \quad g = \begin{bmatrix} m \\ ml/\rho \\ p + m^2/\rho \\ mn/\rho \\ m(p + \varepsilon)/\rho \end{bmatrix}, \quad h = \begin{bmatrix} n \\ nl/\rho \\ nm/\rho \\ p + n^2/\rho \\ n(p + \varepsilon)/\rho \end{bmatrix} \quad (3)$$

A discretization of the flow field into tetrahedral elements is carried out. A piecewise linear representation of the flow variables along each tetrahedral element is used. The flow variables are stored at each node. The piecewise linear representation along each cell allows an exact formulation [8] of the linearized time evolution problem as the superposition of waves corresponding to the eigenmodes of the convective part of the flow equations. The wave propagation directions may be oriented at arbitrary directions in the cell thus allowing true multidimensional transmission of information in a time step. This is sometimes too costly in terms of computer time and a simplified, partially multidimensional approach may be used whereby the residue over a cell is distributed to the cell nodes in accordance with

some scheme reflecting the true wave propagation direction. In contrast with the standard finite volume scheme, Riemann problems along each cell boundary are not solved; the Riemann problem procedure introduces a bias in favor of the boundary normal direction that is avoided in a residual distribution scheme.

The unsteady equations are solved in time. The basic time stepping scheme may be written as

$$q_i^{n+1} = q_i^n + \frac{\Delta t}{S_i} \sum_T \beta_T^i \Phi_T \quad (4)$$

where i is the node index and the sum is carried out over all tetrahedra adjoining the node i . Intermediate time steps, as given by a second order Runge-Kutta scheme, were used in this work. The coefficients β_T^i are called distribution coefficients [3] and satisfy a normalization condition $\sum_{i=1}^3 \beta_T^i = 1$. The fluctuation

$$\Phi_T = - \oint_{S_T} \vec{F} \cdot \vec{n} dA = - \int_{V_T} \vec{\nabla} \vec{F} (u(\vec{x})) dV \quad (5)$$

has been introduced. The coefficients β_T^i specify how much of the fluctuation is to be advected towards node i . The amount to be advected is done in accordance with physical criteria of ensuring upwind dependence. For this an eigenmode decomposition is required. As usual, it is more convenient to find carry out the Euler eigensystem decomposition in the primitive variables $Q = [\rho \ u \ v \ w \ p]^T$ for which the Euler equations are $Q_t + \vec{F}_Q \cdot \vec{\nabla} Q = f$. In this work the generalization of the simple 1-D N distribution [1] of the fluctuation developed in [4] has been adopted. The fluctuation distributed to node i is

$$\Phi_i = M K_i^{Q+} (Q_i - Q_{in}) \quad (6)$$

where $K_i^{Q+} = (A\hat{n}_{x,i} + B\hat{n}_{y,i} + C\hat{n}_{z,i})/2$ and $(\hat{n}_{x,i}, \hat{n}_{y,i}, \hat{n}_{z,i})$ is the inward pointing normal of magnitude equal to the area of a cell face. The reference inflow state Q_{in} is determined by solving

$$\left(\sum_j K_j^- \right) Q_{in} = \sum_j K_j^- Q_j \quad (7)$$

The K^+, K^- matrices refer to the decomposition with respect to the signs of the eigenvalues. The decomposition is carried out in primitive variables and the distributed fluctuations are transformed into conservative variables using the transformation matrix $M = \partial q / \partial Q$.

2.2 Viscous effects

Viscosity effects do not affect the basic multidimensional splitting procedure presented above. These effects are included using a standard Galerkin formulation in

the computation. To ease notation we present the procedure as applied to the simple scalar diffusion equation

$$\frac{\partial u}{\partial t} + \vec{\lambda} \cdot \nabla u = \nu \Delta u \quad (8)$$

The procedure may be easily extended to the full Navier-Stokes equations. Integrating over a control volume (the dual median cell) Ω we obtain

$$\int_{\Omega} \frac{\partial u}{\partial t} \omega_i d\Omega + \int_{\Omega} \vec{\lambda} \cdot \nabla u \omega_i d\Omega = \int_{\Omega} \nu \Delta u \omega_i d\Omega \quad (9)$$

with ω a weight function describing the residual procedure presented above. In order to eliminate the second order derivative (inappropriate in as much as we are using a piecewise linear representation of the flow variables) we integrate by parts

$$\int_{\Omega} \frac{\partial u}{\partial t} \omega_i d\Omega + \sum_T \int_T \vec{\lambda} \cdot \nabla u \omega_i d\Omega = \oint \omega \frac{\partial u}{\partial n} d\partial\Omega - \sum_T \nu \int_T \nabla \omega_i \cdot \nabla u d\Omega \quad (10)$$

The viscosity term contains now only first order derivatives. We introduce a Galerkin representation for the viscous term

$$u = \sum u_i N_i \quad (11)$$

where N_i are the standard shape functions associated with linear interpolation over a cell.

2.3 Turbulence model

The effects of turbulence were included through the dynamic subgrid scale stress (SGS) ideas of Germano [5]. Two filtering operations corresponding to successive levels of the embedded tetrahedral grids are considered. The first is the usual grid filtering operation denoted usually by \cdot . By applying this filter subgrid turbulent stresses appear in the Navier-Stokes equations. These are denoted by τ_{ij} . The second is called a test filter and typically uses a filter width larger (e.g., twice) of the grid filter. The standard notation is $\widehat{\cdot}$. New turbulent SGS stresses appear which shall be denoted by T_{ij} . The turbulent stresses are linked by the Germano identities $\mathcal{L}_{ij} = T_{ij} - \widehat{\tau}_{ij}$ with $\mathcal{L}_{ij} = \widehat{\widehat{u}_i \widehat{u}_j} - \widehat{u}_i \widehat{u}_j$. By applying the same, eddy viscosity turbulence model at both scales a procedure may be established for dynamically computing the eddy viscosity coefficient so as to reflect local flow conditions.

$$\tau_{ij} - \frac{\delta_{ij}}{3} \tau_{kk} = -2C \bar{\Delta}^2 |\bar{S}| \bar{S}_{ij} = -2C \beta_{ij} \quad (12)$$

$$T_{ij} - \frac{\delta_{ij}}{3} T_{kk} = -2C \widehat{\Delta}^2 |\widehat{S}| \widehat{S}_{ij} = -2C \alpha_{ij} \quad (13)$$

Typically, the above equations are used in

$$\mathcal{L}_{ij}^a = \mathcal{L}_{ij} - \frac{\delta_{ij}}{3} \mathcal{L}_{kk} = -2C\alpha_{ij} + 2\widehat{C}\beta_{ij} \quad (14)$$

a system of 5 equations from which C may be determined by a least squares technique for instance [7]. Given that there are no homogeneous directions in the type of flow considered here, the least squares average has been carried out over families of embedded tetrahedra. Though empiric, this procedure has shown accuracy sufficient for engineering computation when applied to LES test cases. In conjunction with the multigrid acceleration procedure we apply the Germano identities at each pair of grid levels in complete V cycle. In effect, the dynamic SGS model is used to provide the restriction and prolongation operators of the multigrid procedure. This has been observed to allow sufficient smoothing of the operators to avoid oscillations in the V cycle computation.

2.4 Resolution requirements

An important aspect of extending LES simulations to the large Reynolds number flows encountered in technical applications is the determination of the appropriate resolution requirements. In the present work a full resolution of the complete turbulent flow field around the rotor blade was too costly in computer resources to carry out. In order to achieve some progress in the investigation of the applicability of the LES technique to practical aerodynamic problems a hybrid approach has been adopted here. Grid refinement criteria were set to ensure full resolution of the boundary layer of the blade. This involves computing the local values of y^+ , u^+ for tetrahedra close (less than a tenth of a chord length) to a solid surface. In this region a more stringent criterion is set for the maximum allowed gradient of the flow variables. Typically, the adaptive grid procedure produces about 12-18 grid points along a normal to the blade surface for the region $y^+ \in [0, 1000]$. Further away from the blade surface the resolution achieved by the grids used in this work are not fine enough to be said to carry out an LES simulation. Rather the turbulence model away from the blade surface is of the eddy-viscosity type. This accounts for some the observed under-resolution of the large scale coherent structures downstream of the blade. The number of nodes varies during the course of the computation since they are dynamically added and deleted in order to satisfy imposed gradient requirements.

3 Application to a twisted NACA 0012 rotor

The procedures outlined above are applied to a rotor blade undergoing a vertical descent at an angle of $\alpha = 20^\circ$. The blade is of rectangular planform between radii $R_0 = 0.5$ m și $R_1 = 6.0$ m. The airfoil chord is $b = 0.2$ m and the rotational speed is $\Omega = 50$ rad/s. The helicopter forward velocity is $V = 20$ m/s. The blade is considered rigid but with a total torsion of 20° from hub to tip. The blade rotation plane is

rotated by $\gamma = -10^\circ$ with respect to the forward flight direction. To visualize the flow field we choose five sections as outlined in the following table:

Section	R (m)	Local angle of attack	Mach	Reynolds
1	0.500	10°	0.07	$0.5 \cdot 10^7$
2	1.875	15°	0.23	$1.6 \cdot 10^7$
3	3.250	20°	0.47	$3.2 \cdot 10^7$
4	4.625	25°	0.72	$4.9 \cdot 10^7$
5	6.000	30°	0.88	$6.0 \cdot 10^7$

The exterior computational boundary is limited by two parabolic cylinders whose extremal coordinates are $(-5,0)$, $(10,0)$, $(5,10)$, $(5,-10)$ in planes perpendicular to the blade span. The computational domain is constructed by carrying out a Delaunay triangularization in 100 planes perpendicular to the span. Corresponding nodes in two adjacent planes are then joined in order to form a triangular base prism. This is afterwards split into two tetrahedra. A sample section through the grid is presented in figure 1. The average number of nodes during the computation was $1.63 \cdot 10^6$. A dual CPU workstation with 256 MB of memory and sustained rate of 74 MFLOPS was used. The full computation required 148 hours.

The flow is visualized by presentation of lines of constant pressure and Mach number (fig. 2,3). The figures presented below were constructed for $\psi = 0^\circ$. Investigation of the flow results reveal the following

1. the flow is transonic starting from $R = 4.1$ m;
2. the tip mean flow is steady;
3. a periodic shedding of vorticity is seen to occur on an inboard portion of the rotor blade from $R = 1.72$ m at $R = 2.14$ m;

4 A BVI example

We now consider an example of the blade-vortex interaction problem. We are interested in the possibility of controlling noise emissions by using porous airfoils. In order to get a preliminary assesment of this effect we shall carry out an essentially two-dimensional simulation with the span dimension reduced to single layer of ancestor cells. This imposes a spatial resolution cutoff for the turbulent eddies along the span. The single layer of ancestor cells was chosen to be 1/10 of the chord in depth. The modification of the turbulence fluctuations by the airfoils porosity is an unknown effect at present. The numerical simulation attempted here is intended as a first attack on this problem.

A NACA 0012 airfoil at zero incidence is subjected to a flow perturbation induced by a vortex of nondimensional intensity $\Gamma = -0.05$ (reference units are the upstream flow velocity and the blade chord) of radius $r = 0.5$. The Reynolds number is taken $Re = 10^5$.

Porosity is modeled by imposing the boundary conditions

$$\vec{v} \cdot \vec{n} = V_n, \quad \vec{v} \cdot \vec{t} = 0 \quad (15)$$

over selected portions of the airfoil. In the present simulation two portions of 0.02 chordwise extent were considered; one is positioned at $x = 0.85$ the other at $x = 0.2$. The pressure difference between these two stations drives a flow through the airfoil itself. This flow is assumed to be governed by Darcy's law

$$Q = kA \frac{\Delta p^*}{L} \quad (16)$$

The porosity coefficient was taken as $k = 10^{-2}$. The perturbation induced upon the mean flow is evidenced by comparison of the following two iso Mach line plots. There is a perceptible weakening of the shock when porous flow is considered (fig. 4,5). The interest for aeroacoustic applications is whether the effect is important and stable enough to lead to an overall reduction in emitted noise.

The aerodynamic data that has been obtained is now used to estimate the acoustic signature in the far field at a distance of 20 chords from the leading edge at 4 angular positions $\alpha = 0, 30, 60, 90$ degrees as shown in fig. 6.

The acoustic field is computed using the Kirchhoff surface technique. The integral

$$4\pi p(\vec{x}, t) = \int_S \left[\frac{p}{r^2} \frac{\partial r}{\partial n} - \frac{1}{r} \frac{\partial p}{\partial n} + \frac{1}{a_0 r} \frac{\partial r}{\partial n} \frac{\partial p}{\partial \tau} \right]_{\tau} dS. \quad (17)$$

is evaluated numerically by using the approximation

$$4\pi p(\vec{x}, t) = \sum_{i=1}^N \left[\frac{p}{r^2} \frac{\partial r}{\partial n} - \frac{1}{r} \frac{\partial p}{\partial n} + \frac{1}{a_0 r} \frac{\partial r}{\partial n} \frac{\partial p}{\partial \tau} \right]_{\tau, i} \Delta S_i \quad (18)$$

Here τ is the retarded time, $\tau = t - r/a_0$ and \vec{r} is the vector from a point on the Kirchhoff surface to the observation point. The Kirchhoff surface is taken as circle of radius 7 enclosing the airfoil. The acoustic signatures obtained for the two cases – solid and porous airfoils – are presented in fig. 7.

The following conclusions may be drawn:

1. There is a modest (10-15%) decrease in the peak acoustic pressures for the porous airfoil;
2. the acoustic signal increases in length;
3. the spectral content of the acoustic signal is increased.

These effects are though at this stage to be mainly caused by the lag in re-establishment of the shock position on the suction side of the airfoil.

5 Conclusions

A novel numerical procedure for the simulation of unsteady rotor flows has been presented. The procedure presents the following advantages:

1. Ability to treat general geometric shapes by use of an unstructured discretization;
2. Multidimensional numerical scheme (i.e., not based on dimensional splitting), thus minimizing spurious numerical modes;
3. Self adjusting, dynamic turbulence model.

References

- [1] Special course on unstructured grid methods for advection dominated flows. Technical report, AGARD Report 787, 1992.
- [2] AGARD. A selection of test cases for the validation of large-eddy simulations of turbulent flows. Technical Report 345, AGARD, 1998.
- [3] H. Deconinck, R. Struijs, H. Bourgois, H. Paillere, and P. Roe. Multidimensional upwind methods for compressible flows. *AGARD*, R-787, 1992.
- [4] E. V. der Weide and H. Deconinck. Upwind residual distribution methods for compressible flow: An alternative to finite volume and finite element methods. part ii: System schemes and applications. In *28th CFD Lecture Series*, Bruxelles, Belgium, 1997. Von Karman Institute for Fluid Dynamics.
- [5] M. Germano, U. Piomelli, P. Moin, and W. Cabot. A dynamic subgrid-scale eddy viscosity model. *Phys. Fluids*, A 3:1760, 1991.
- [6] S. Mitran, D. Caraeni, and D. Livescu. Large eddy simulation of unsteady rotor-stator interaction in a centrifugal compressor. In *33rd AIAA/ASME/SAE/ASEE Joint Propulsion Conference and Exhibit*, New York, 1997. AIAA.
- [7] U. Piomelli and J. Liu. Large-eddy simulation of rotating channel flows using a localized dynamic model. *Phys. Fluids*, 7:839–848, 1995.
- [8] P. L. Roe. Discrete models for the numerical analysis of time-dependent multi-dimensional gas dynamics. *J. Comp. Phys.*, 63:458–476, 1986.

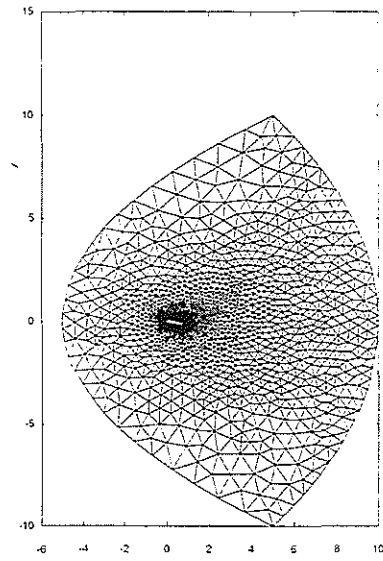


Fig. 1. Section through the computational grid at rotor hub, $R = 0.5$ m (angle of attack $\alpha = 10^\circ$).

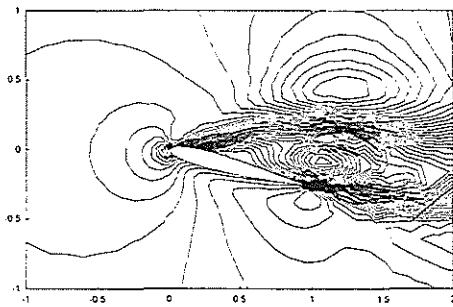


Fig. 2. Iso-Mach lines in Section 2 at $\alpha = 15^\circ$ showing detached hub flow.

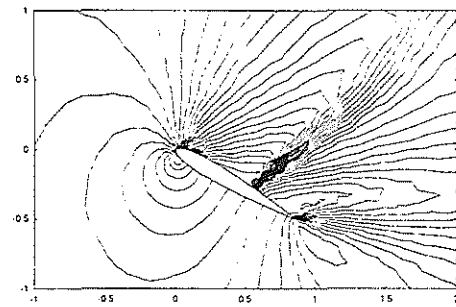


Fig. 3. Iso-Mach lines in Section 5 at $\alpha = 30^\circ$ showing transonic tip flow.

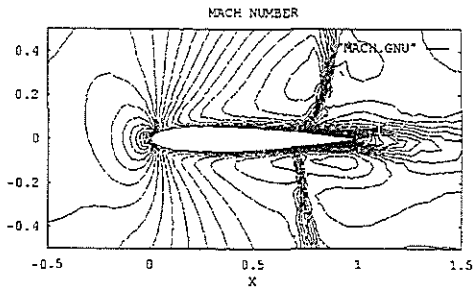


Fig. 4. Izo-Mach lines, vortex-blade interaction computation, solid airfoil.

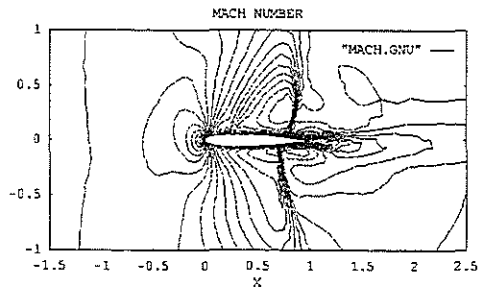


Fig. 5. Izo-Mach lines, vortex-blade interaction computation, porous airfoil, same physical time as previous figure..

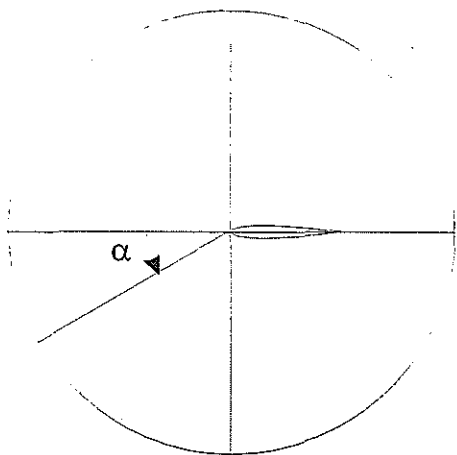


Fig. 6. Points used in evaluation of acoustic field from BVI.

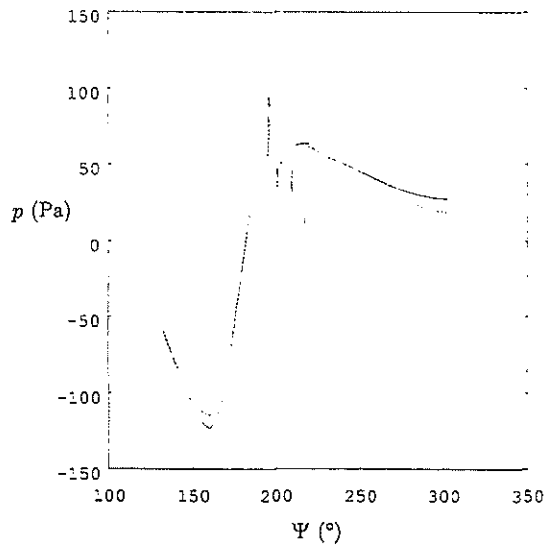


Fig. 7. Acoustic pressure at $\alpha = 0$ degrees (continuous line - solid airfoil, dotted line - porous airfoil).